Proceedings of the Nineteenth (2009) International Offshore and Polar Engineering Conference
Osaka, Japan, June 21-26, 2009

ISBN 978-1-880653-53-1 (Set); ISSN 1098-618

Numerical Simulation of Liquid Sloshing in LNG Tanks Using a Compressible Two-Fluid Flow Model

Y. G. Chen, W. G. Price and P. Temarel
Ship Science, School of Engineering Sciences, University of Southampton
Southampton, UK

ABSTRACT

In this investigation the Reynolds-Averaged Navier-Stokes (RANS) equations are modified to account for variable density and viscosity of the two-fluids flow (i.e. water-air), assuming both fluids compressible. By introducing a preconditioner, the governing equations in terms of primitive variables are solved for both fluids in a unified manner. The non-conservative implicit Split Coefficient Matrix Method (SCMM) is modified to approximate convective flux vectors in the dual time formulation. The free surface waves inside the tank, due to sloshing, are implicitly captured by using a level set approach.

The method is illustrated through applications to rectangular and chamfered tanks subject to sway or roll motions at different filling levels and excitation conditions (i.e. amplitude and frequency of oscillation). Comparisons are made between calculated and experimental pressures, where available.

KEY WORDS: Sloshing, impact pressure, compressible interface flow, level set method, LNG tank.

INTRODUCTION

The Liquefied Natural Gas (LNG) carrier is often dubbed as the pearl of the shipbuilding industry as the technology required is very demanding and complicated. Due to energy demands, increasing numbers of LNG carriers are required. The need for larger cargo capacity, coupled to the demand for more flexible operations, provide the stimulus for design changes in these vessels. There are, by and large, two types of LNG carrier tanks, namely Moss-type and membrane-type. Since LNG vessels with membrane type tanks are often the first choice for new very large vessels and as, unlike the Moss-type tanks, they experience large sloshing pressures on tank boundaries, the issue of sloshing induced pressure loads in membrane tanks has become more important than ever. The possibility of sloshing damage has already attracted much attention in the LNG industry today.

In the case of shallow filling and severe sea-induced motions a hydraulic jump forming a vertical front may be generated, resulting in very large impacts on tank walls. On the other hand, in a nearly full tank, the excited progressive wave may cause high stresses acting on its roof (Mikelis et al, 1984). The fluid impacts on the tank walls and roof are extremely localized in time and space because of the large temporal and spatial pressure gradients. Due to the very short duration of the impact pressure the accurate and stable assessment of the impulsive impact load remains a challenging task (Arai et al, 2002). Over the past few decades great efforts have been made to estimate numerically sloshing-induced pressure loads exerted on tank walls and roof, with increasing accuracy of tracing or capturing highly nonlinear free surface configurations such as wave overturning, breaking and merging. The numerical techniques most used include Marker and Cell (MAC) (Armenio and Rocca, 1996), Volume of Fluid (VOF) (Wemmenhove et al, 2007), Level Set (LS) (Price and Chen, 2006; Chen et al, 2009) and Smoothed Particle Hydrodynamics (SPH) (Delorme et al, 2009) methods.

Experiments (e.g. Rognebakke and Faltinsen, 2005; Lugni et al, 2006) have revealed that the compressibility of air has significant effects on impact pressure as trapped air, depending on the dimensions of air bubbles, may prolong the duration of the impact peak and change its magnitude. A mathematical model including gas compressibility is expected to result in better understanding and more accurate predictions of sloshing induced impacts.

It is customary to model compressible two-phase flow by employing the fully compressible Navier-Stokes equations and a different equation of state for each phase. The change in equations of state, due to the difference of their specific heat ratios, is known to cause spurious pressure oscillations in numerical solutions for compressible multi-fluids flow in conservative form near the interface (Koren et al, 2002). In addition, the standard methods adopted to solve compressible flows, based on hyperbolic conservation laws, are neither numerically robust nor efficient in the case of low Mach numbers (Turkel, 1999). In this investigation a preconditioning technique is introduced to solve low speed compressible two-fluid flows occurring in liquid sloshing in an enclosed container. The non-conservative implicit Split Coefficient Matrix Method (SCMM) is modified to approximate convective flux vectors in a dual time formulation. The level set formulation is employed to implicitly capture free surface waves generated due to sloshing. The mathematical model, including compressibility, is applied to rectangular and chamfered tanks, at different filling levels, subject to externally imposed sway or roll motions. Numerically predicted

pressures on tank boundaries are compared with available experimental measurements.

MATHEMATICAL FORMULATION

Governing Equations

The fluid motion in liquid and gas phases are both assumed to be compressible. This two-fluid system is assumed immiscible, adiabatic and fluid density ρ is only a function of pressure p, e.g. $\rho = \rho(p)$. The continuity and momentum equations governing both gas and liquid motions are combined to form a single equation system in the vector form

$$\Gamma \frac{\partial q}{\partial \tau} + \frac{\partial Q}{\partial t} + \frac{\partial e_j}{\partial x_j} - \frac{\partial e_j^v}{\partial x_j} = -s \tag{1}$$

where

$$q = (p, u, v, w)^T, \quad Q = (\rho, \rho u, \rho v, \rho w)^T,$$

$$e_j = (\rho u_j, \rho u u_j + p, \rho v u_j + p, \rho w u_j + p)^T,$$

$$e_j^v = \frac{\mu}{\mathrm{Re}}(0, \frac{\partial u}{\partial x_j} + \frac{\partial u_j}{\partial x}, \frac{\partial v}{\partial x_j} + \frac{\partial u_j}{\partial y}, \frac{\partial w}{\partial x_j} + \frac{\partial u_j}{\partial z})^T,$$

$$s = \rho(0, f_1 + g_1/Fn^2, f_2 + g_2/Fn^2, f_3 + g_3/Fn^2)^T.$$

In equation (1), the spatial coordinates x_j, velocity components u_j and components of the gravitational acceleration along the axes g_i, have been non-dimensionalized for each specific problem in terms of a characteristic length L, a characteristic velocity U_0 and gravitational acceleration g, respectively. The fluid density ρ and viscosity μ are non-dimensionalized by their equivalent values in water, ρ_w and μ_w, respectively, whereas time t and pressure p by L/U_0 and $\rho_w U_0^2$, respectively. Re and Fn represent Reynolds and Froude numbers, respectively, and are defined as

$$\mathrm{Re} = LU_0/\nu_w, Fn = U_0/\sqrt{Lg}, \tag{2}$$

where ν_w denotes the kinematic viscosity.

In addition to the gravitational force, the external forces also include the translational and rotational inertia forces, and f_i takes the following form

$$f_i = a_i + \varepsilon_{ijk}\frac{d\omega_j}{dt}x_k + \varepsilon_{ijk}\varepsilon_{klm}\omega_j\omega_l x_m + 2\varepsilon_{ijk}\omega_j u_k, \tag{3}$$

where a_i represents the translational acceleration components and ω_i the rotational angular velocity components. The Levi-Civita symbol is denoted by ε_{ijk}, with repeating subscripts indicating a summation. The effect of surface tension is neglected in this mathematical model.

In equation (1), a preconditioning technique is introduced by adding the derivative terms with respect to a pseudo-time variable τ to this system. Thus, each previous equation contains two sets of time derivatives. The variable t represents the real physical time. To optimize the performance of the pseudo-iteration, the preconditioning step consists of the replacement Γ by a matrix and this process is defined by

$$\Gamma = \begin{bmatrix} 1/V_r^2 & 0 & 0 & 0 \\ u/V_r^2 & \rho_\varepsilon & 0 & 0 \\ v/V_r^2 & 0 & \rho_\varepsilon & 0 \\ w/V_r^2 & 0 & 0 & \rho_\varepsilon \end{bmatrix}.$$

Here V_r is the reference velocity,selected to ensure the system is well conditioned at low speed and to accelerate convergence. In practice, this parameter is generally defined as a combination of the free-stream and the local convective velocity as suggested by Turkel (1999).

Equation (1) can be rewritten in vector form, using the generalized coordinates, as

$$\Gamma \frac{\partial \tilde{q}}{\partial \tau} + \frac{\partial \tilde{Q}}{\partial t} + \frac{\partial \tilde{e}_j}{\partial \xi_j} - \frac{\partial \tilde{e}_j^v}{\partial \xi_j} = -\tilde{s} \tag{4}$$

where vectors $\tilde{q}, \tilde{Q}, \tilde{e}^j, \tilde{e}_v^j$ and $\tilde{s}$ are expressed as

$$\tilde{q} = J^{-1}q, \tilde{Q} = J^{-1}Q, \ \tilde{s} = J^{-1}s$$

$$\tilde{e}_j = J^{-1}(\rho U_j, \rho u U_j + \frac{\partial \xi_j}{\partial x}p, \rho v U_j + \frac{\partial \xi_j}{\partial y}p, \rho w U_j + \frac{\partial \xi_j}{\partial z}p)^T$$

$$\tilde{e}_j^v = J^{-1}\frac{\mu}{\mathrm{Re}}\frac{\partial \xi_j}{\partial x_m}(0, \frac{\partial \xi_k}{\partial x_m}\frac{\partial u}{\partial \xi_k} + \frac{\partial \xi_k}{\partial x}\frac{\partial u_m}{\partial \xi_k}, \frac{\partial \xi_k}{\partial x_m}\frac{\partial v}{\partial \xi_k} + \frac{\partial \xi_k}{\partial y}\frac{\partial u_m}{\partial \xi_k}, \frac{\partial \xi_k}{\partial x_m}\frac{\partial w}{\partial \xi_k} + \frac{\partial \xi_k}{\partial z}\frac{\partial u_m}{\partial \xi_k})^T.$$

Here $J = \partial(\xi, \eta, \zeta)/\partial(x, y, z)$ is the Jacobian of the transformation and the contra-variant velocity component U_j is defined by

$$U_j = \frac{\partial \xi_j}{\partial x_m}u_m.$$

Our current goal is to simulate fluid sloshing problems encountered in the field of ship hydrodynamics, so gas and liquid are both assumed to be adiabatic. The densities are updated by means of an equation of state. In this study, the Tait equation of state is employed for water and the ideal gas equation of state for air. Both have the following form:

$$\frac{p + B}{p_0 + B} = \left(\frac{\rho}{\rho_0}\right)^\gamma \tag{5}$$

where p_0 and ρ_0 are the reference pressure and density values, respectively. B and γ are both constants, with values $B = 296.3 \times 10^{+6}$ and $\gamma = 7.415$ for water, and $B = 0$ and $\gamma = 1.4$ for air. With reference to equation (5), the speed of sound for each phase is calculated from the following equation

$$c = \sqrt{\frac{\partial p}{\partial \rho}} = \sqrt{\frac{\gamma(B + p)}{\rho}}.$$

Free surface capturing method

The free surface is defined as the zero level set of a level-set function ϕ initialized as a signed distance function from the interface. In air ϕ is set to a positive value and in water to a negative value defined by

$$\begin{cases} \phi(x_i, t) > 0 & \text{in} \quad \text{air}, \\ \phi(x_i, t) = 0 & \text{on} \quad \text{surface}, \\ \phi(x_i, t) < 0 & \text{in} \quad \text{water}. \end{cases} \tag{6}$$

Differentiating $\phi = 0$ with respect to t, a transport equation is derived to describe the free surface motion in the form

$$\frac{\partial \phi}{\partial t} + u_i \frac{\partial \phi}{\partial x_i} = 0, \tag{7}$$

where u_i is the local fluid velocity and, at any time, moving the interface is equivalent to updating ϕ by solving equation (7).

Due to sharp variations of fluid properties at the free surface, there is the need to introduce a region of finite thickness 2ε over which smooth but rapid change of density and viscosity occurs, across the interface.

A smoothed Heaviside function $H_\varepsilon(x)$, introduced by Sussman et al (1994), is defined, such that

$$H_\varepsilon(x) = \begin{cases} 1 & \text{if } x > \varepsilon \\ 0 & \text{if } x < -\varepsilon \\ 0.5(x+\varepsilon)/\varepsilon + 0.5\sin(\pi x/\varepsilon)/\pi & \text{otherwise.} \end{cases} \tag{8}$$

Using the above function, we define the corresponding smoothed density ρ and viscosity μ functions

$$\rho_\varepsilon(\phi) = (1 - H_\varepsilon(\phi)) + \frac{\rho_a}{\rho_w} H_\varepsilon(\phi), \tag{9}$$

$$\mu_\varepsilon(\phi) = (1 - H_\varepsilon(\phi)) + \frac{\mu_a}{\mu_w} H_\varepsilon(\phi). \tag{10}$$

Even if we initialize ϕ as a signed distance from a wave front (or interface), the level set function no longer remains a distance function at later times. An iterative procedure, called re-initialization, is used at each time step by solving a Hamilton-Jacobi equation to ensure ϕ satisfies $|\nabla \phi| = 1$ (Sussman et al, 1994). During the re-initialization exercise a process is introduced to preserve the fluid volume in each cell and improve the accuracy of solution to equation (7) (Sussman et al, 1998).

NUMERICAL METHOD

Implicit temporal discretization

Adopting an implicit Euler back-forward difference formula to approximate the pseudo-time derivative and a second-order, three-point, backward-difference implicit formula to approximate the time derivative, equation (4) can be expressed as

$$\Gamma \frac{\widetilde{q}^{m+1,n+1} - \widetilde{q}^{m,n+1}}{\Delta \tau} + \frac{1.5\widetilde{Q}^{m+1,n+1} - 2\widetilde{Q}^{n} + 0.5\widetilde{Q}^{n-1}}{\Delta t} + \delta_\xi \widetilde{e}^{m+1,n+1} = 0, \tag{11}$$

where, for the sake of simplicity, the convective flux derivative only in one direction is written, and the viscous and source terms in equation (4) are omitted. This approach is adopted henceforward. For example, we denote $\widetilde{e}$ to represent the convective flux $\widetilde{e}_1$ in the ξ-direction.

In equation (11), the superscript n denotes the n^{th} physical time level, the superscript m the level of sub-iteration and δ_ξ represents a spatial difference. After linearizing terms at the $(m+1)^{\text{th}}$ time level and involving some simple algebraic manipulation, equation (11) becomes

$$(\Gamma + M\frac{3\Delta\tau}{2\Delta t} + A_q \Delta\tau\, \delta_\xi)\delta_\tau \widetilde{q} + \delta_\xi \widetilde{e}^{m,n+1} = \widetilde{r}^{m,n+1}, \tag{12}$$

where δ_τ represents the time difference, $M = \frac{\partial \widetilde{Q}}{\partial \widetilde{q}}$, $A_q = \frac{\partial \widetilde{e}}{\partial \widetilde{q}}$, and

$$\widetilde{r}^{m,n+1} = -\frac{1.5\widetilde{Q}^{m,n+1} - 2\widetilde{Q}^{n} + 0.5\widetilde{Q}^{n-1}}{\Delta t}.$$

Let us define $\Gamma_d = \Gamma + M\frac{3\Delta\tau}{2\Delta t}$ as the non-conservative variable preconditioning matrix. Multiplying both sides of equation (12) by the inverse Γ_d^{-1} results in

$$(I + \Gamma_d^{-1} A_q \Delta\tau\, \delta_\xi)\delta_\tau \widetilde{q} + \Gamma_d^{-1} A_q \delta_\xi \widetilde{q} = \Gamma_d^{-1} \widetilde{r}, \tag{13}$$

where it is easily verified that the preconditioned flux Jacobian matrix is given by

$a_q = \Gamma_d^{-1} A_q$.

Spatial discretization

The basic idea behind the non-conservative SCMM scheme is to split the Jacobian coefficient matrix into two sub-matrices, each associated with the positive or negative eigenvalues of the Jacobian (Chakravarthy et al, 1980). Hence, a one-sided finite difference scheme can be applied to each split flux difference.

Multiplying both sides of equation (13) by Γ_d and implementing the similarity transform for the Jacobian matrix $a_q = T\Lambda T^{-1}$ leads to

$$(\Gamma_d + \Delta\tau\, \Gamma_d T\Lambda T^{-1}\delta_\xi)\delta_\tau \widetilde{q} + \Gamma_d T\Lambda T^{-1}\delta_\xi \widetilde{q} = \widetilde{r}. \tag{14}$$

Here the diagonal matrix Λ consists of the eigenvalues of a_q, and T is the matrix of its right eigenvectors.

Implementing positive and negative decomposition of the Jacobian matrix and defining the positive and negative non-conservative flux differences as

$$\delta_\xi \widetilde{e}^{+} = \Gamma_d T\Lambda^{+}T^{-1}\delta_\xi \widetilde{q} = \Gamma_d a_q^{+}\delta_\xi \widetilde{q} = \overline{a}_q^{+}\delta_\xi \widetilde{q},$$

$$\delta_\xi \widetilde{e}^{-} = \Gamma_d T\Lambda^{-}T^{-1}\delta_\xi \widetilde{q} = \Gamma_d a_q^{-}\delta_\xi \widetilde{q} = \overline{a}_q^{-}\delta_\xi \widetilde{q},$$

equation (14) can be expressed in the form

$$(\Gamma_d + \Delta\tau\, \overline{a}^{+}\delta_\xi + \Delta\tau\, \overline{a}^{-}\delta_\xi)\delta_\tau \widetilde{q} = \widetilde{r} - \delta_\xi \widetilde{e}^{+} - \delta_\xi \widetilde{e}^{-}, \tag{15}$$

where the plus (minus) eigenvalue matrices are given by

$$\Lambda^{\pm} = \frac{1}{2}(\Lambda \pm |\Lambda|).$$

The first order upwind difference approximation to the positive and negative flux differences at a node j is

$$\delta_\xi \widetilde{e}^{+} + \delta_\xi \widetilde{e}^{-} \approx \overline{a}_q^{+}(\overline{q}_{j-1/2})(\widetilde{q}_j - \widetilde{q}_{j-1}) + \overline{a}_q^{-}(\overline{q}_{j+1/2})(\widetilde{q}_{j+1} - \widetilde{q}_j), \tag{16}$$

where $\overline{q}_{j+1/2}$ is the arithmetic average of the primitive variables $\widetilde{q}_j$ and $\widetilde{q}_{j+1}$.

The second order upwind and third order upwind-biased methods were derived by Lombard et al (1983). Here the fourth order upwind-biased scheme is given as follows

$$\begin{aligned} &\frac{3}{4}\overline{a}_q^{+}(\overline{q}_{j+1/2})\delta_\xi \widetilde{q} + \frac{13}{12}\overline{a}_q^{+}(\overline{q}_{j-1/2})\delta_\xi \widetilde{q} - \frac{11}{12}\overline{a}_q^{+}(\overline{q}_{j-3/2})\delta_\xi \widetilde{q} + \frac{1}{12}\overline{a}_q^{+}(\overline{q}_{j-5/2})\delta_\xi \widetilde{q} \\ &+ \frac{3}{4}\overline{a}_q^{-}(\overline{q}_{j-1/2})\delta_\xi \widetilde{q} + \frac{13}{12}\overline{a}_q^{-}(\overline{q}_{j+1/2})\delta_\xi \widetilde{q} - \frac{11}{12}\overline{a}_q^{-}(\overline{q}_{j+3/2})\delta_\xi \widetilde{q} + \frac{1}{12}\overline{a}_q^{-}(\overline{q}_{j+5/2})\delta_\xi \widetilde{q} \\ &+ \frac{1}{3}\overline{a}_q^{-}(\overline{q}_{j-1/2})\delta_\xi \widetilde{q} + \frac{5}{6}\overline{a}_q^{-}(\overline{q}_{j+1/2})\delta_\xi \widetilde{q} - \frac{1}{6}\overline{a}_q^{-}(\overline{q}_{j+3/2})\delta_\xi \widetilde{q}. \end{aligned} \tag{17}$$

COMPUTATIONAL RESULTS

Numerical simulations were carried out for a selection of model tanks subject to forced roll or sway motions and the predicted pressures are compared with experimental data, where available. Unless otherwise stated, the mediums are assumed to be air and water with density of water $\rho_w = 1025\, kg/m^3$. In equation (5), the reference density and pressure of air are $\rho_0 = 1.0\, kg/m^3$ and $p_0 = 10^{+5}\ \mathrm{N/m^2}$, respectively. It is assumed the fluid is inviscid and a slip boundary condition is applied to the rigid walls of the tank including the roof. The effect of surface tension is neglected in this investigation.

Case A: 2D rectangular tank with roll motion

Fig. 1 shows rectangular tank used in case A. This is a longitudinal section of a membrane type tank from a 138000m^3 LNG carrier, at a scale of 1:50. The time history of roll motion, with an approximate amplitude of 4º, is slightly different from a simple harmonic function, as it is impossible to start with infinite acceleration. The rolling axis is 18.4cm above the base line of the tank. The measured data was supplied by the Naval Architecture Department of the Technical University of Madrid, as reported by Delorme et al (2008).

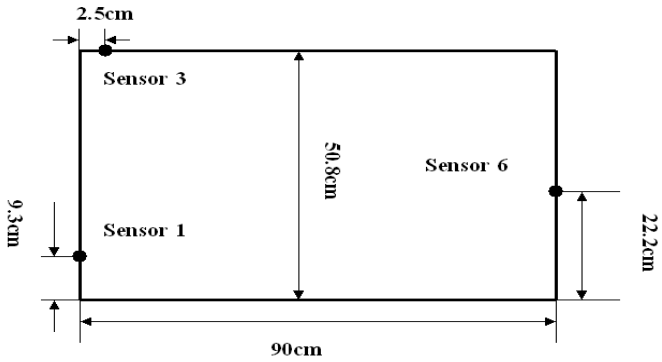

Fig. 1: Tank geometry and position of the sensors for Case A

Numerical simulation was carried out at a filling level of 44% corresponding to 22.2cm from base line and an exciting period $T=T_0=1.32$s (where T_0 denotes the first sloshing natural period based on linearized theory). The computational conditions are: Mesh size 91×51, time step 5×10^{-4}s and $2\varepsilon=3\Delta z$, where Δz is the vertical distance between two adjacent grid nodes. Fig. 2 shows comparisons of the time history of calculated pressure at sensors 3 (a) and 6 (b) with the corresponding measured data. It can be seen that the first and second peak values of impact pressure are correctly captured but overestimated compared to experimental measurements recorded at sensor 6. There is a good agreement between calculated and measured impact pressures at sensor 3, when the water is impacting the roof of the tank.

Case B: Chamfered tank with roll motion

For case B, sloshing motion was assessed in a chamfered model tank at 30% filling level (see Fig. 3). The real tank dimensions and roll motion are described in Table 1.

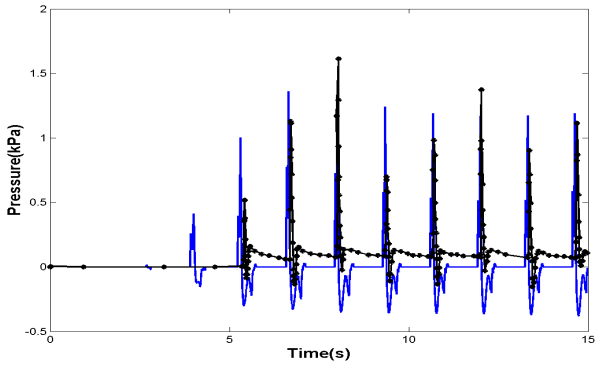

(a)

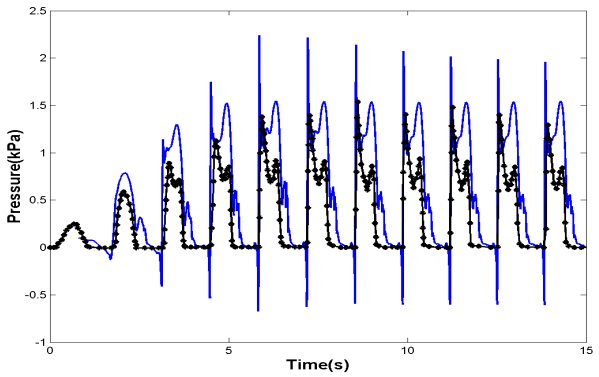

(b)

Fig.2 Comparisons of pressure time histories between calculated and measured data at sensors (a) 3 and (b) 6 for Case A; solid lines denote predictions and symbols measured data.

In the current numerical investigation the 2D tank, at model scale, is used to simulate liquid sloshing. Pressure at positions 258 to 261 were calculated during the numerical simulation, for which experimental data are available. Time histories of calculated and measured pressures at position 261 are presented in Fig. 4, showing good overall agreement between predicted and measured peak pressures. Results for other positions also show similar agreement, but not shown here due to the rather small pressure values.

Table 1 Real tank dimensions and motion characteristics for case B

Dimensions (units: m)
Length: 39.12 Breadth: 43.82 Height: 29.08
Upper chamfer height: 9.584 Lower chamfer height: 4.284
Upper chamfer angle: 45° Lower chamfer angle: 45°
Motion
Roll motion: 5°,
Roll period: 9.5 s;
Centre of rotation: 14.10 m above tank bottom

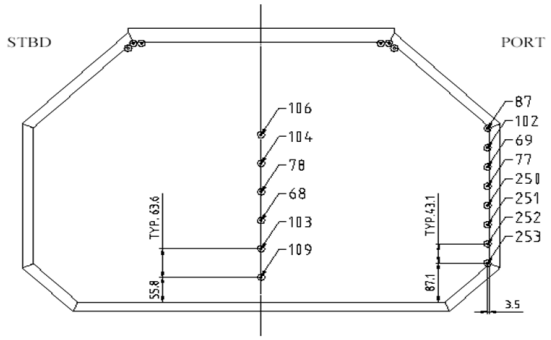

(a) Bulkhead

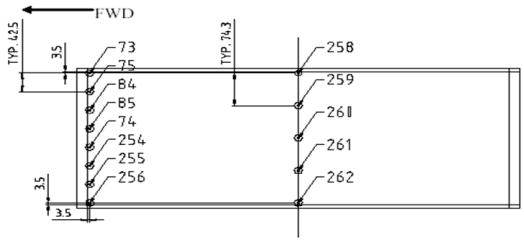

(b) Port side

Fig. 3 Setup of 3D model tank for Case B (unit: mm)

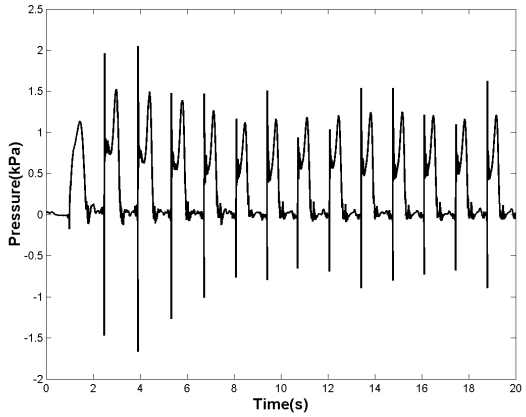

(a) Calculated

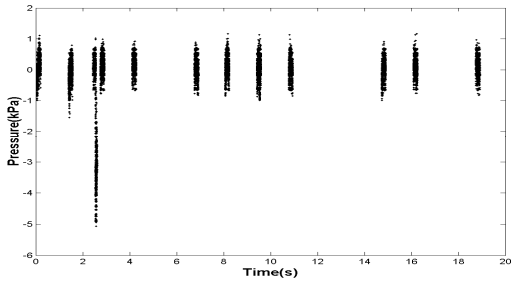

(b) Measured

Fig. 4 Comparison of pressure time histories between (a) calculated and (b) measured data at position 261 for Case B

Case C: 2D chamfered tank with sway motion

In this section, a chamfered model tank is used to further simulate liquid sloshing, to be used by the ISOPE-2009 Technical Program Committee for the comparative study in the Sloshing Dynamics Symposium. The calculated results for only two cases are presented here. The distributions of pressure sensors are shown in Fig.5. The dimensions of the tank, positions of pressure gauges and the frequencies and amplitudes of sway motion are given in Table 2. The sway motion at the start of the test is in the opposite direction to the side where the sensors are located.

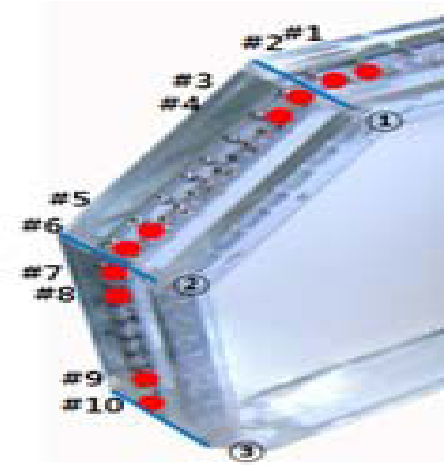

Fig. 5 Distribution of ten pressure sensors for Case C

Table 2 Tank dimensions, sensor positions and sway motion characteristics for Case C

Tank dimensions		Sensors	Distance*
Length	1.516m	1	108mm
Breadth	0.14m	2	28mm
Height	1.0703m	3	28mm
Upper chamfer	0.34668m	4	108mm
Lower chamfer	0.1511m	5	108mm
Upper chamfer angle	45°	6	28mm
Lower chamfer angle	45°	7	28mm
Thickness of tank wall	40mm	8	108mm
Diameter of sensor	6.5mm	9	108mm
		10	28mm

Filling level	Frequency of motion	Amplitude of motion
20%	0.4632Hz	151.6mm
70%	0.6861Hz	151.6mm

*Distance is along the tank median line from its closest edge marked by (1), (2) or (3) in Fig. 5

Table 3 Computational conditions for sloshing simulations for Case C

Case no.	Mesh size	Density ratio	Filling level
C-1(1)	45×55	1:1025	20%
C-1(2)	45×55	2:1025	20%
C-1(3)	61×65	1:1025	20%
C-2(1)	45×55	1:1025	70%
C-2(2)	81×85	1:1025	70%

These are blind tests; hence, only calculated results without experimental data are presented and analysed here. The sensitivity of sloshing induced impact pressure is also investigated by changing mesh

size and ullage density. The time step increments for all test cases in this section are set to 5×10^{-4}s. The remaining computational conditions used for modelling sloshing for both filling levels are summarized in Table 3. The comparison of the time histories of calculated pressure at sensors 9 and 10 using two different density ratios of gas and liquid (Cases C-1(1) and C-1(2) in Table 3) for 20% filling case are shown in Fig. 6. It is obvious that there is no significant difference on impact pressure when ullage density changes from one to two. This implies that impact pressure is not sensitive to gas-liquid density ratio. The conclusion is also supported by Lee et al (2007). For this reason, in subsequent calculations, an ullage value of one is assumed. Nevertheless, further work is required to find the critical point in the tank when the density ratio has a significant effect on impact pressures.

Case C-1(3) with a mesh resolution of 61×65 is used to investigate numerically the first impact event, taking place in this case when the wave front is moving towards and then hitting the right hand side wall of the tank, namely the side opposite to the one fitted with sensors. Fig. 7 depicts the details of this impact event for the 20% filling case. The vectors in Fig.7 denote the velocities of both fluids, scaled for adequate visibility in water; hence, resulting in large velocity depictions in air, with the vectors unavoidably overflowing the tank boundaries. It can be seen from Frame 1 (t1=2.35s) that a hydraulic jump with a vertical wall forms and moves towards the left-hand side wall. Due to the high speed of the wave front the wave crest overturns in Frame 2 (t2=2.575s). Then the wave crest and trough move towards each other and a small cavity is nearly trapped during this stage, shown in Frame 3 (t3=2.665s). The wave moves rapidly and closer to the wall which can be seen from the nearby air movement. Finally impact takes place, shown in Frame 4 (t4=2.675s). It is found that the impact occurs just below or at the mean free surface (denoted by the solid line in Fig. 7). The numerical results also show that the impact is happening just before the tank reaches its maximum amplitude of motion (i.e. when the sway displacement is about 0.151m). A sudden turning of the flow forces the liquid to move upwards along the wall and form a rapid jet, as seen in Frame 5 (t5=2.6925s). Due to gravity the rising jet drops after it reaches its top point, as shown in Frame 7 (t7=3s). Examining frames 4 to 7 it is clear to see that, when the liquid is transported from right to left, the cavity is forced to move up and its shape also changes. Its size and shape is expected to have a significant effect on the amplitude and duration of the impact pressure.

In order to record the pressure variation during the first impact event, six positions on the right hand side wall of the tank were investigated. Four of these positions, referred to as 5r, 6r, 9r and 10r are the counterparts to sensors 5, 6, 9, and 10. The other two positions 11 and 12 are located at the right lower chamfer, at distances of 28mm and 108mm, respectively, from edge 3 along the tank median line (see Fig. 5). Fig. 8 shows the short time history of the first impact pressure exerted at positions 9r, 10r, 11 and 12 during this impact event. Pressures at positions 5r and 6r are not shown, as they are relatively small. The contraction and expansion of the compressible air cavity cause the observed high frequency pressure oscillations.

Following the first impact event, the tank is moved in the opposite direction. Then the motion of the liquid inside the tank will follow a similar process to that shown in Fig.7, forming a hydraulic jump which may result in overturning and creating cavities or/and bubbles during the violent sloshing and finally hitting the left hand side wall leading to the formation of a high speed vertical jet. Fig. 9 shows the time history of impact pressure on sensors 9 and 10 during this following impact. The pressure oscillation frequency and amplitude in Fig. 9 are different from those in Fig. 8. One possible explanation is that the sizes, shapes and locations of the two cavities are different. The event sequence shown in Fig.7 and the pressure time histories in Figs. 8 and 9 illustrate the importance of the effects of air compressibility, included in the current work, on wave impacting during sloshing. Nevertheless, further investigations are required to obtain more evidence.

For the 70% filling level calculated pressure histories at sensors 1 to 8 are shown in Figs. 10-13, illustrating the effects of two different mesh sizes, namely 45×55 and 81×85. Examining these figures, it is noted that pressure peaks calculated using the finer mesh are a little higher than those obtained using the cruder mesh. Nevertheless, both models provide similar main features for the impact pressures. This is a high filling case and the flow is very violent. Further work is required to investigate the characteristics of phenomena such as flow spray and the formation of cavities at the top corner of the tank. In Fig. 10 the impact pressure acting on sensor 1 is much higher than that of sensor 2. This may be explained as a result of the violent motion of the fluid leading to a massive water move upwards, whilst simultaneously hitting a relatively large area of the roof. In addition, from Fig. 12 it is shown again that impact on a vertical wall occurs near the mean free surface.

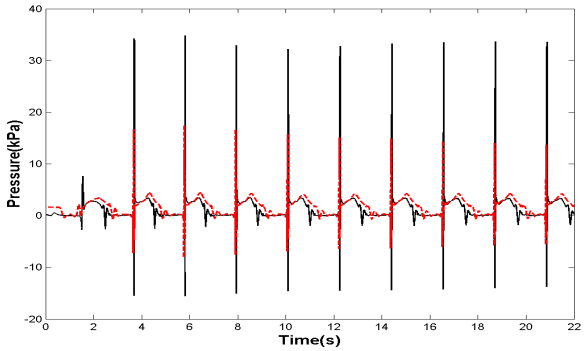

(a) Case C-1(1): density ratio=1:1025

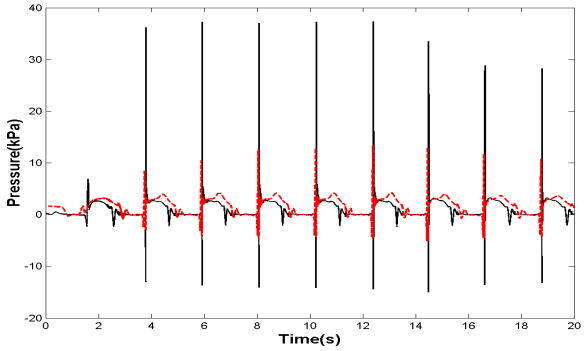

(b) Case C-1(2): density ratio=2:1025

Fig. 6 Comparison of calculated pressure time histories at sensors 9 and 10 using two different density ratios for 20% filling level (solid line: sensor 9; dotted line: sensor 10)

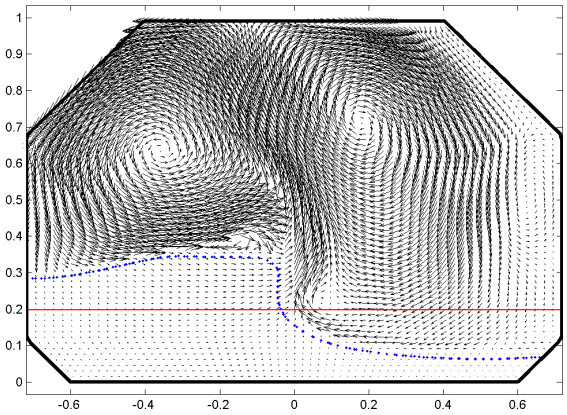

Frame 1 (t1=2.35s)

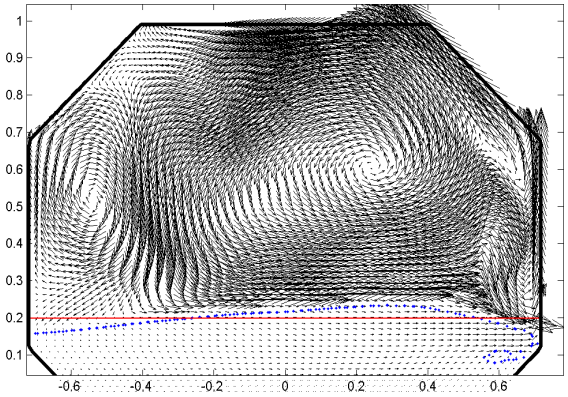

Frame 4 (t4=2.675s)

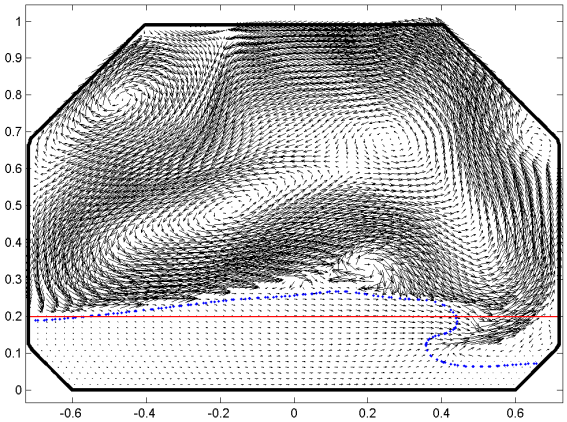

Frame 2 (t2=2.575s)

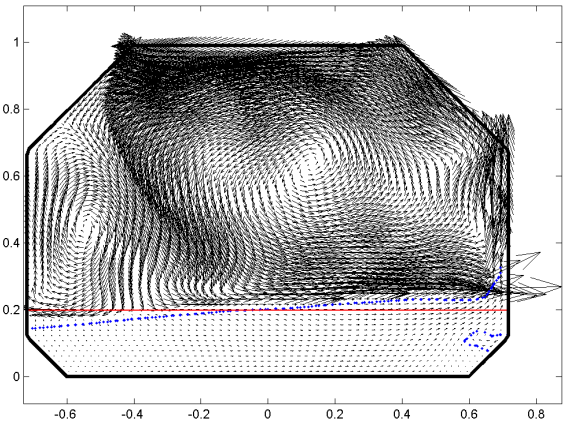

Frame5 (t5=2.6925s)

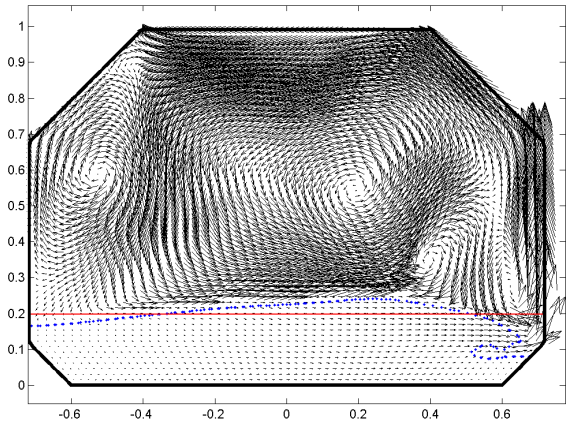

Frame 3 (t3=2.665s)

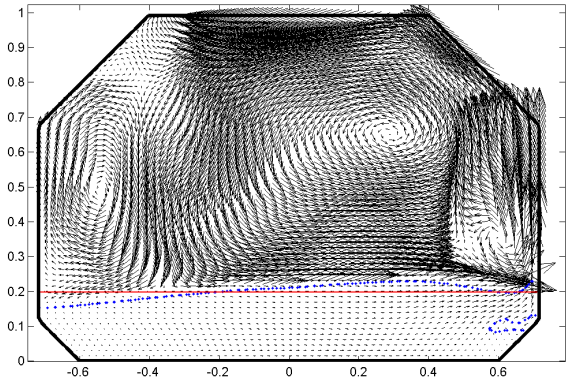

Frame 6 (t6=2.725s)

Fig.7 (continued overleaf)

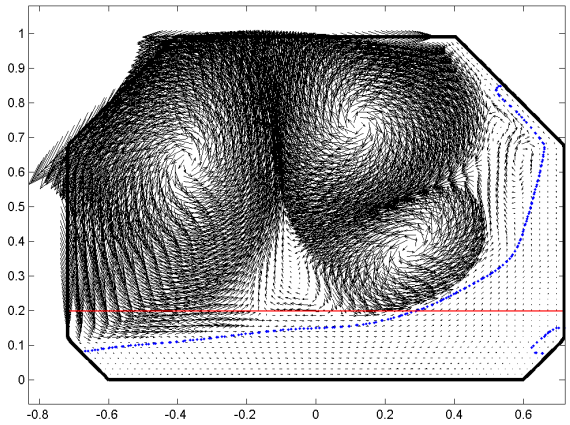

Frame 7 (t7=3.0s)

Fig. 7 Sequence of images at various time intervals during the first impact showing free surface evolution for Case C-1(3); solid and dashed lines denote the mean free surface and fluid interface, respectively

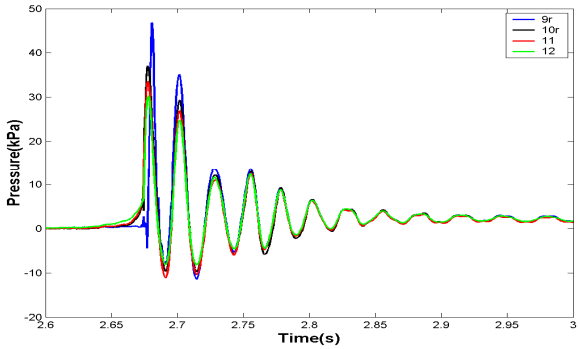

Fig. 8 Pressure time history due to cavity compressibility during the first impact event at points 9r, 10r, 11, 12; 20% filling level (Case C-1(3))

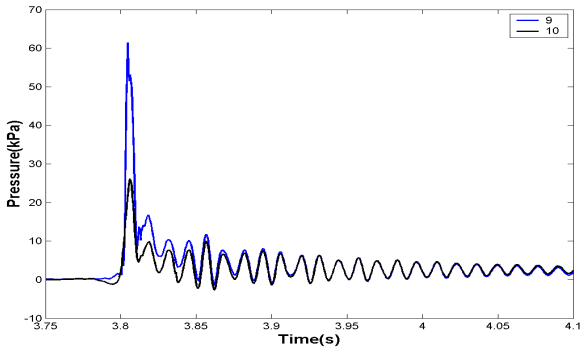

Fig. 9 Pressure time history due to cavity compressibility for the event following the first impact event (see Fig.8) at points 9, 10; 20% filling level (Case C-1(3))

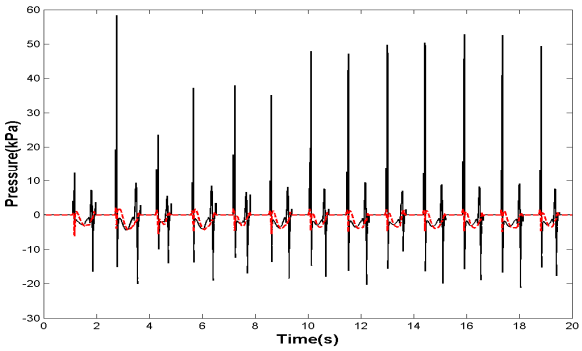

(a) Case C-2(1) (Mesh size: 45×55)

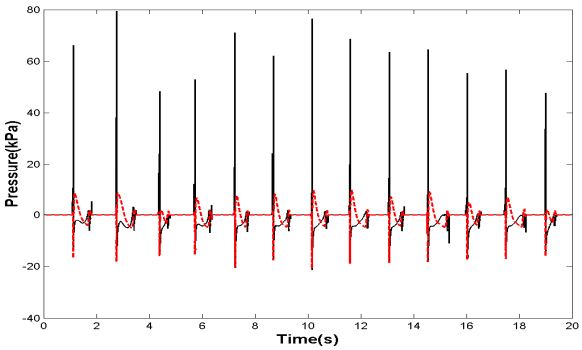

(b) Case C-2(2) (Mesh size: 81×85)

Fig. 10 Comparison of pressure time histories calculated at sensors 1 and 2 using two different mesh sizes for 70% filling level (solid line: sensor 1; dotted line: sensor 2)

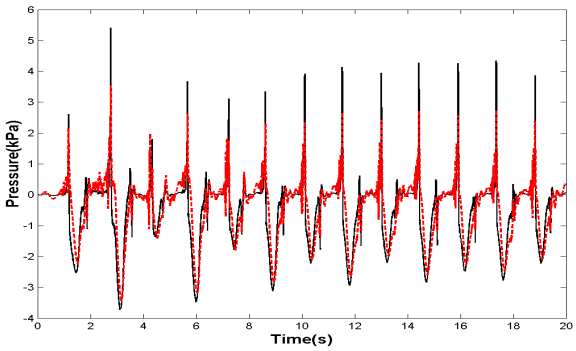

(a) Case C-2(1) (Mesh size:45×55)

Fig.11 (continued overleaf)

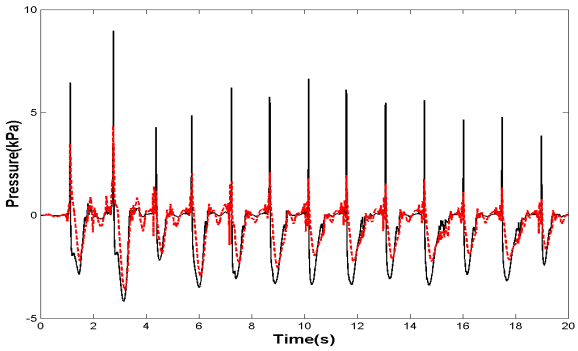

(b) Case C-2(2) (Mesh size: 81×85)

Fig. 11 Comparison of pressure time histories calculated at sensors 3 and 4 using two different mesh sizes for 70% filling level (solid line: sensor 3; dotted line: sensor 4)

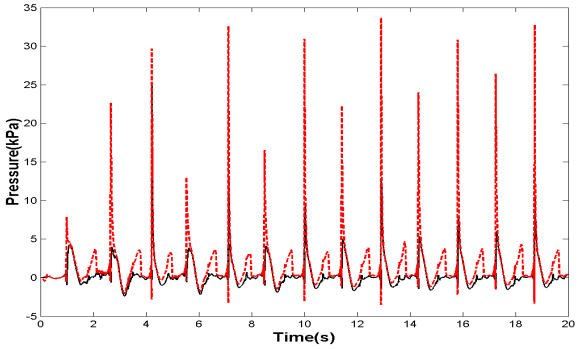

(a) Case C-2(1) (Mesh size:45×55)

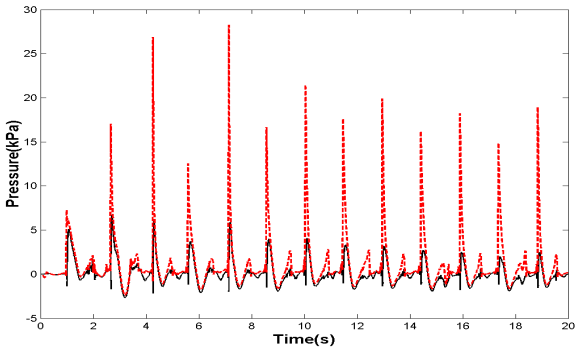

(b) Case C-2(2) (Mesh size:81×85)

Fig. 12 Comparison of pressure time histories calculated at sensors 5 and 6 using two different mesh sizes for 70% filling level (solid line: sensor 5; dotted line: sensor 6)

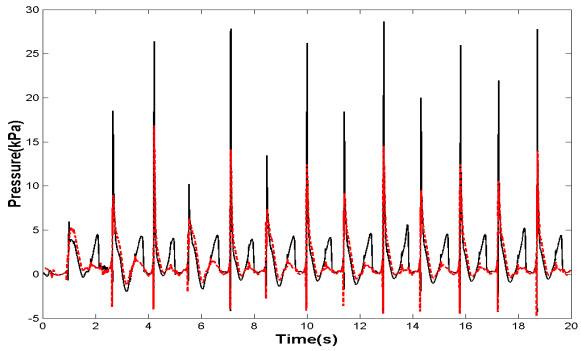

(a) Case C-2(1) (Mesh size:45×55)

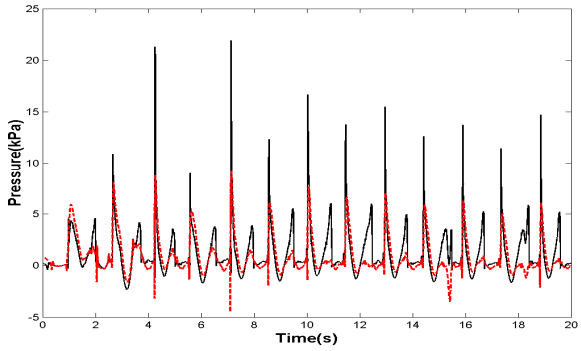

(b) Case C-2(2) (Mesh size:81×85)

Fig. 13 Comparison of pressure time histories calculated at sensors 7 and 8 using two different mesh sizes for 70% filling level (solid line: sensor 7; dotted line: sensor 8)

CONCLUSIONS

The developed numerical method for computing compressible two-fluid flows has been applied to simulate liquid sloshing in a range of partially filled containers. From the limited numerical tests it can be concluded that the current method provides an acceptable level of accuracy for sloshing induced impact pressure exerted on tank walls and roof.

Liquid sloshing is a complex phenomenon as air is often trapped in the impacting zone forming air bubbles or a mixture of air and water. Air compressibility has a significant effect on the behavior of wave impacting pressure. Occurrence of a hydraulic jump and cavity were illustrated using one example of the chamfered tank, Case C. Further investigations are needed to study the mechanism of wave impacting during sloshing.

In this study very limited numerical tests were conducted. There is no doubt that a finer grid is required to simulate the violent free surface motion such as wave overturning, breaking and merging. The dependencies of time and mesh resolution on impact pressure need to be investigated in our further work

ACKNOWLEDGEMENT

The authors gratefully acknowledge the support from Lloyd's Register Educational Trust University Technology Centre in Hydrodynamics, Hydroelasticity and Mechanics of Composites at the University of Southampton.

REFERENCES

Arai, M, Cheng, LY, Kumano, A, and Miyamoto, T (2002). "A technique for stable numerical computation of hydrodynamic impact pressure in sloshing simulation," Journal of the Society of Naval Architects of Japan 191, 299.

Armenio, V, and Rocca, ML (1996). "On the analysis of sloshing of water in rectangular containers: numerical study and experimental validation," Ocean Engineering 23, 705.

Chakravarthy, SR, Anderson, DA, and Salas, MD (1980). "The split coefficient matrix method for hyperbolic systems of gasdynamic equations," AIAA 80-0268.

Chen, YG, Djidjeli, K, and Price, WG (2009). "Numerical simulation of liquid sloshing phenomena in partially filled containers," Comput. Fluids, 38, 830..

Delorme, L, Colagrossi, A, Souto-Iglesias, A, Zamora-Rodriguez, R, and Botia-Vera, E (2009). "A set of canonical problems in sloshing, Part I: Pressure field in forced roll--comparison between experimental results and SPH," Ocean Engineering, 36, 168.

Koren, B, Lewis, MR, van Brummelen, EH and van Leer, B (2002). "Riemann-problem and level set approaches for homentropic two-fluid flow computations," J. Comput. Phys. 181, 654.

Lee, DH, Kim, MH, Kwon, SH, Kim, JW, and Lee, YB (2007). "A parametric sensitity study on LNG tank sloshing loads by numerical simulations," Ocean Engineering, 34, 542.

Lombard, CK, Bardina, J, Venkatapathy, E, and Oliger, J (1983). "Multi-dimensional formulation of CSSM – an upwind flux difference eigenvector split method for the compressible Navier – Stokes equations," AIAA 83-1895.

Lugni, C, Brocchini, M, and Faltinsen, OM (2006). "Wave impact loads: The role of the flip-through," Phys. Fluids 18, 122101.

Mikelis, NE, Miller JK, and Taylor, KV (1984). "Sloshing in partially filled liquid tanks and its effect on ship motions: numerical simulation and experimental verification," Transactions of the Royal Institution of Naval Architects 126, 267.

Price, WG, and Chen, YG (2006). "A simulation of free surface waves for incompressible two-phase flows using a curvilinear level set formulation," International Journal for Numerical Methods in Fluids 51, 305.

Rognebakke, O, and Faltinsen, OM (2005). "Sloshing induced impact with air cavity in rectangular tank with a high filling ratio," 20th International Workshop on Water Waves and Floating Bodies, Spitsbergen, Norway.

Sussman, M, Fatemi, E, Smereka, P, and Osher, S (1998). "An improved level set method for incompressible two-phase flows," Computers & Fluids, 27, 663.

Sussman, M, Smareka, P, and Osher, S (1994). "A level set approach for computing incompressible two-phase flows," J. Comput. Phys. 14, 146.

Turkel, E (1999). "Preconditioning techniques in computational fluid dynamics," Annu. Rev. Fluid Mech. 31, 385.

Wemmenhove, R, Loots, E, and Veldman, AEP (2007). "Numerical simulation of sloshing in LNG tanks with a compressible two-phase model," 26th International Conference on Offshore Mechanics and Arctic Engineering, San Diego, USA.